Monolayers and self-assembled bilayers on ITO for use in solar cells

Kardula, Jane

DOI:
10.33612/diss.1082120674

3

CARBAZOLE BILAYERS ON ITO FOR HYBRID PEROVSKITE SOLAR CELLS

Abstract: *This chapter explores the use of monolayers and self-assembled bilayers (SABs) as an alternative to PEDOT:PSS. Our findings indicate that using* ***Br-2PACz*** *as a monolayer results in low wettability of the active material. However, introducing a SAB made of* ***Br-2PACz*** *and* ***4CzNH$_3$I*** *enhances wettability due to the presence of the ammonium moiety on the surface. Additionally, this SAB leads to better performance and higher stability of the solar cells with a narrower distribution of results.*

The contents of this chapter have been published as "Self-assembled Bilayer to Tune the Surface Energy of Hole Transport Layers Based on Carbazole SAMs for Highly Efficient Sn/Pb- Perovskite Solar Cells" by Matteo Pitaro, Javier E. Sebastián Alonso, Lorenzo Di Mario, David Garcia Romero, Karolina Tran, Jane Kardula, Teodor Zaharia, Malin B. Johansson, Erik M. J. Johansson, Ryan C. Chiechi, Maria Antonietta Loi in Advanced Functional Materials.

3.1. INTRODUCTION

Hybrid perovskite solar cells containing Pb have made significant progress, achieving a PCE over 25 % from just 9 % since 2012.[1,2] However, concerns about the potential environmental impact of Pb leakage are still being investigated within the research community. Studies have explored methods of encapsulating the Pb, the impact of external factors on the solar cell module, and the effects of Pb leakage on soil and human health.[3–9]

Researchers have been exploring the possibility of using Sn as a substitute for Pb in hybrid perovskite solar cells, as it is a suitable candidate. According to a study by Filippetti *et al.*, the theoretical PCE for Sn-based hybrid perovskites is 32.3 %, which is higher than the 30.5 % for Pb-based hybrid perovskites.[10] However, actual PCE values for pure Sn hybrid perovskite thin films have been below 10 %, and may even be less than 5 %, due to the ease with which Sn can oxidize from Sn^{2+} to Sn^{4+}. This oxidation leads to unintentional hole doping, causing a Moss-Burstein effect, an increase in optical band gap, and a blue shift in emission.[11–13] To counteract this oxidation, researchers have used quantum rods or heterogeneous 2D/3D structures for the hybrid perovskite active layers, or doping with SnF_2. While SnF_2 improves the PCE to 15 %, this PCE is still lower than the performance of lead-based hybrid perovskites.[14–16] This result led researchers to explore partial exchange of Pb with Sn, which has shown to be a viable option for achieving high PCE and better stability. In a study by Hu *et al.*, an inverted architecture was used to achieve an efficiency of 23.6 % and maintain 80 % of device performance after 200 h of continuous operation.[17]

The most commonly used p-type material in this architecture is PEDOT:PSS, but its acidity and hygroscopic properties can lead to stability and performance issues.[18–24] Researchers have explored using self-assembled monolayers (SAMs) by spin-coating reactive molecules onto a substrate. However, this method can result in partially formed SAMs and disordered aggregates due to the rapid evaporation of solvents during spin-coating. Kinetically trapped, disordered SAMs of apolar molecules counterintuitively increase the wettability of polar surfaces such as ITO, while well-ordered, densely-packed SAMs decrease it.[25–27] When using a hybrid perovskite precursor solution with polar solvents to apply the active material, it will more readily cover a partially formed, disordered SAM than a non-polar, well-ordered and densely-packed SAM. SAMs can be anchored through either non-covalent interactions or covalent bonds. The main difference between the two is that non-covalent SAMs are dynamic and tend to reorganize themselves continuously to minimize their free energy, forming dense and well-organized domains. On the other hand, covalent SAMs, like those formed by spin-coating Phosphonic acids (PAs) on ITO to make selective contacts, are not dynamic and cannot reorganize themselves once formed.

To ensure the formation of well-ordered, densely-packed covalent-SAMs, we incubate the activated substrates in a solution of the phosphonic acids overnight instead of introducing them during spin-coating. We chose **Br-2PACz** decorated with a phosphonic acid anchoring group attached to the carbazole via a two-carbon spacer because the parent 2PACz is known to facilitate the extraction of charge from the perovskite layers, while the short linker provides sufficient flexibility to form a well-ordered covalent-SAMs without increasing the contact resistance. Due to the relationship between order and

wettability, the well-ordered, densely-packed covalent SAM of **Br-2PACz** led to poor wettability, undermining their beneficial charge-transport properties. We solved this problem by introducing a second, non-covalent SAM of **4NH$_3$CzI** on top of **Br-2PACz**, creating a self-assembled bilayer (SAB). The formation of bilayers is driven by the need to minimize interfacial free energy. When **4NH$_3$CzI** is added, it passivates the **Br-2PACz** SAM and introduces ionic groups to the surface, increasing its wettability. The enthalpy of π-π stacking of the carbazole moieties helps to stabilize the bilayer by reducing its internal energy. Additionally, the top SAM is not covalently bound to the surface, making it dynamic. As the hybrid perovskite layer crystallizes, the top SAM continuously reorganizes to minimize interfacial free energy and reduce surface defects that can contribute to surface non-radiative recombination.

3.2. RESULTS & DISCUSSION

To obtain **4NH$_3$CzI** (**3**), we began by reacting commercially available carbazole with 1,4-dibromobutane under basic conditions to produce **1**. Next, we reacted **1** with di-tert-butyliminocarboxylate (HNBoc$_2$) in a similar S_N2 fashion to obtain intermediate **2** in a quantitative yield. Finally, we converted the Boc-protected amine to the desired ammonium iodide under acidic conditions using HI in a two-step reaction. First, we deprotected the Boc-protected amine to the free amine, followed by another reaction to obtain the final product **3** (**Scheme 3.1**).

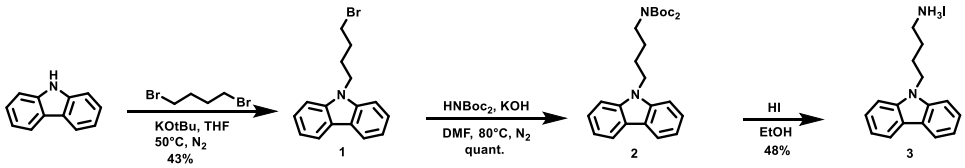

Scheme 3.1 Reaction scheme for synthesis of 4-(9H-carbazol-9-yl)butan-1-amonium iodide (**4NH$_3$CzI,(3)**. Starting with carbazole, it reacted with 1,4-dibromobutane under basic conditions to obtain **1**, followed by reaction with HNBoc$_2$ prior to deprotection and formation of the desired product **3**.

After synthesizing **4NH$_3$CzI** and prior to forming the bilayer, we cleaned the ITO substrates and treated them in an oven and UV-O_3 to remove any organic contaminants on the surface. Next, we dipped the substrates in a 0.1 m M solution of **Br-2PACz** and washed them twice the following day using 100 µL of EtOH while spinning to remove any non-covalently bonded **Br-2PACz**. After that, we deposited a solution of **3** (0.5 mg mL^{-1}) on top of the samples (ITO/**Br-2PACz**) and left it for 1 to 2 minutes. Finally, we spun the samples at 3000 rpm and dried them at 100 °C to 120 °C to form the SABs. Our research indicates that the SABs are created by minimizing the interfacial free energy, which causes the ammonium moiety to face away from ITO. This leads to a passivation of the **Br-2PACz** monolayer and an increase in surface wettability due to the presence of ionic groups at the ambient interface. To confirm our hypothesis that the ammonium moiety of **4NH$_3$CzI** is facing away from ITO and not integrated into the **Br-2PACz** monolayer, we utilized Kelvin Probe Force Microscopy (KPFM) to measure the work-functions of the various layers (**Figure 3.1**). The work-function increased by 0.94 eV in the case of

the SAB, which indicates that the ammonium group is indeed present at the ambient surface.

We conducted a comparison of the contact angle between the covalently bonded **Br-2PACz** monolayer and the SAB using a hybrid perovskite solution ($Cs_{0.25}FA_{0.75}Sn_{0.5}Pb_{0.5}I_3$) to form a droplet, to support the theory further. The **Br-2PACz** monolayer has its phosphonate group covalently bonded to the ITO surface, with the carbazole moiety pointing away from the surface. As a result, the contact angle is higher. On the other hand, we enhanced the hydrophilicity of the SAB surface to facilitate the sample coating. This was evident from the smaller contact angle and complete coverage of the perovskite on the SAB (**Figure 3.2**).

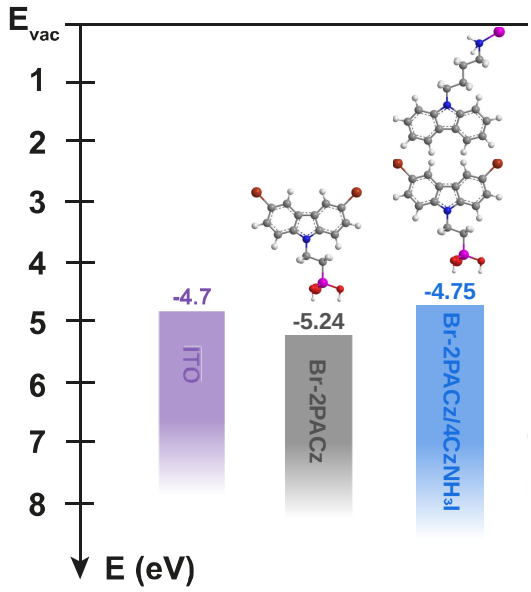

Figure 3.1 KPFM measurements of the work-functions of ITO (purple), ITO with a monolayer **Br-2PACz** (grey), and ITO with SAB (blue).

We used AFM (**Figure 3.3**) to study the surface morphology of ITO, ITO/**Br-2PACz**, and ITO/SAB. The AFM images of ITO and the monolayer of **Br-2PACz** displayed minimal differences in roughness with similar RMS values of 2.25 nm and 2.35 nm, respectively. However, the roughness was reduced by half by forming the SAB, which had a RMS value of 1.103 nm.

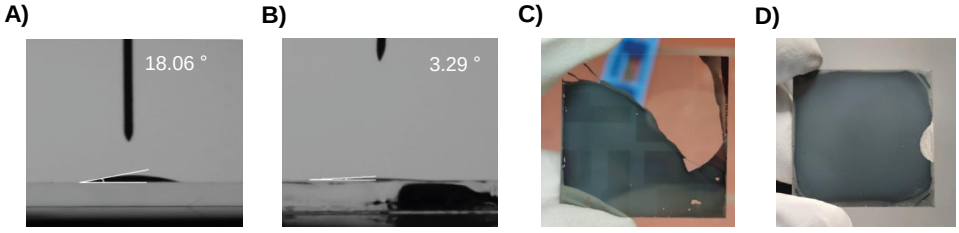

Figure 3.2 Contact angle measurements using $Cs_{0.25}FA_{0.75}Sn_{0.5}Pb_{0.5}I_3$ droplet on**A)** ITO/**Br-2PACz**, **B)** ITO/SAB **C)** Coverage of the hybrid perovskite layer on ITO/**Br-2PACz**, **D)** Coverage of the hybrid perovskite layer on ITO/SAB.

Both champion solar cell devices performed similarly in terms of current density ($\mathbf{J_{sc}}$) and fill factor (**FF**), but differed in open-circuit voltage ($\mathbf{V_{oc}}$) (**Table 3.1**). The device with SAB had a higher V_{oc} due to fewer traps at the interface between SAB and the hybrid

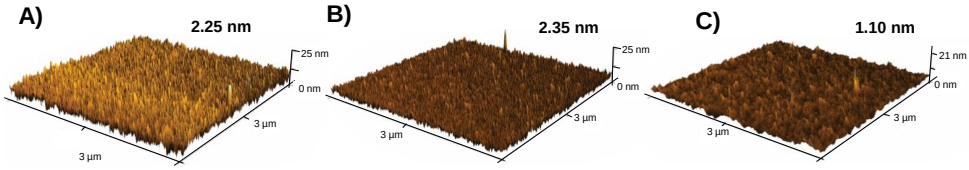

Figure 3.3 AFM images of **A)** ITO with RMS = 2.25 nm, **B)** ITO with **Br-2PACz** monolayer with RMS = 2.35 , **C)** ITO with **Br-2PACz** and **4 CzNH$_3$I** SAB with RMS = 1.10 nm.

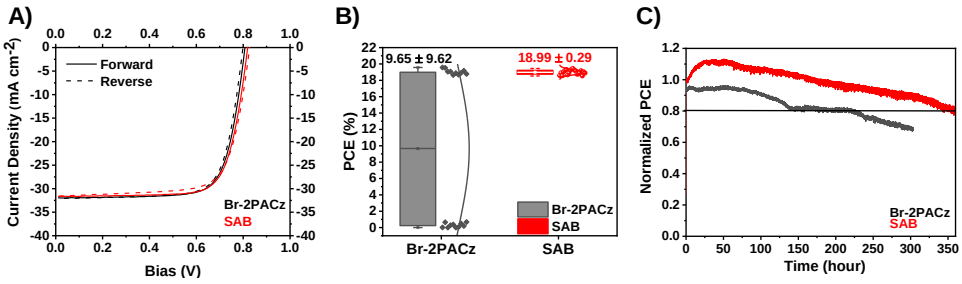

Figure 3.4 A) J-V curves of solar cell device using **Br-2PACz** monolayer and using SAB, **B)** Device statistics using **Br-2PACz** monolayer and SAB, **C)** Performance of devices using **Br-2PACz** monolayer and SAB.

Device	J_{sc} (mA cm^{-2})	V_{oc} (V)	FF	PCE (%)
Br-2PACz	31.95	0.807	0.75	19.34
SAB	31.61	0.819	0.75	19.45

Table 3.1 Comparison of performance of champion devices using **Br-2PACz** monolayer and SAB.

perovskite layer. Adding **4 NH$_3$CzI** to improve wettability did not negatively affect performance, but only had minimal differences in J_{sc}, V_{oc}, FF, and PCE. However, it did improve device reproducibility as shown in **Figure 3.4**. The PCE for the batch of 20 devices with **Br-2PACz** monolayer had high variation with an average of 9.65 ± 9.62, while the SAB batch had a narrower variation of 18.99 ± 0.29. Devices with SAB also had higher operational stability, lasting 132 hours longer than those with only the monolayer due to reduced oxidation of Sn^{2+} to Sn^{4+}, reduced charge carrier recombination, and reduced trap density.

3.3. CONCLUSION

To address the literature reported degradation issue in hybrid perovskite caused by the hygroscopic and acidic nature of PEDOT:PSS, we used a **Br-2PACz** monolayer. However using this monolayer alone can cause problems with the wettability and deposition of the active layer. To solve this, we added a dynamic second monolayer made from **4NH$_3$CzI** that is not covalently bonded. This allows **4NH$_3$CzI** to reorganize during the crystalization of the active layer, resulting in improved device statistics and reproducibility compared to using just the **Br-2PACz** monolayer. Additionally, the ammonium moiety in **4NH$_3$CzI** increased the hydrophylicity of the substrate, which facilitated full film coverage of the perovskite solution.

We have found that using **Br-2PACz** monolayers based on carbazole moiety has several advantages over traditional materials like PEDOT:PSS that can cause degradation of the hybrid perovskite layer due to their hygroscopic and acidic nature. However, the use of the monolayer can create issues with the active layer's wettability. To overcome this issue, we introduced a dynamic second monolayer made from **4NH$_3$CzI** that is not covalently bonded, which allows it to reorganize during the active layer's crystallization. This resulted in improved device statistics and reproducibility compared to devices using just the monolayer. The ammonium moiety in **4NH$_3$CzI** also increased the hydrophilicity of the substrate, which facilitated full film coverage of the hybrid perovskite solution. Furthermore, we also showed that using SAB as a p-type layer greatly increases the stability of the device, with the champion device using SAB retaining 80 % of its performance for 358 hours, compared to 226 hours using **Br-2PACz** monolayer. Comparing the performance of devices using the monolayer and SAB, we can conclude that introducing SAB greatly increases device reproducibility and stability.

3.4. EXPERIMENTAL

All reagents were purchased from Sigma-Aldrich, Acros, TCI Europe and used as received unless otherwise stated. Anhydrous THF, DMF were obtained from an in-house Solvent Purification System. For thin layer chromatography (TLC) Merc silica gel 60 F_{254} aluminium plates were used. Visualization of compounds by TLC were done by irradiation with UV light, I_2, $KMnO_4$ or PMA stain. Column chromatography was performed using a Silicagel Kieselgel 60 M(0.04 – 0.063 mm, 230 – 400 mesh). ^{1}H NMR, ^{13}C NMR were performed on Agilent Technologies 400/54 Premium Shielded (400MHz), Varian Oxford AS400 (400MHz) nuclear magnetic resonance spectrometer. The following abbreviations were used to explain NMR peak multiplicities: s = singlet, d = doublet, t = triplet, q = quartet, m = multiplet, br = broad. High resolution mass spectra (HRMS) was recorded on Thermo Scientific LTQ Orbitrap XL (ESI^+, ESI^-, APCI).

9-(4-bromobutyl)-9H-carbazole (1) A Schlenk tube was charged with 9H-carbazole (1 g ,5.98 mmol, KOtBu (1.3 eq. 0.812 g, 7.77 mmol) and anhydrous THF (10 mL) under inert N_2 atmosphere. After 30 minitues of stirring 1,4-dibromobutane (1.5eq. , 1.91 g, 8.85 mmol) was added and stirred at 55 °C for 24 hours. The crude mixture was washed with water, brine, extracted with CH_2Cl_2 and dried over $MgSO_4$. The crude mixture was purified using silica chromatography using Pentane:CH_2Cl_2 (80:20 v/v %) to obtain the desired product (0.78 g, yield 43 %).

^{1}H NMR (400 MHz, $CDCl_3$) δ 8.1 (d, J = 7.8 Hz, 2H), 7.5 – 7.4 (m, 2H), 7.4 (d, J = 8.2 Hz, 2H), 7.2 (d, J = 7.3 Hz, 2H), 4.4 (t, J = 6.9 Hz, 2H), 3.4 (t, J = 6.5 Hz, 2H), 2.1 (p, J = 7.0 Hz, 2H), 2.0 – 1.9 (m, 2H). ^{13}C NMR (101 MHz, $CDCl_3$) δ 140.8, 126.2, 123.4, 120.9, 119.4, 109.0, 42.7, 33.6, 30.7, 28.1. HRMS - ESI^+ (m/z) Calculated for $C_{16}H_{17}BrN$ $[M+H]^+$: 302.05389 Measured: 302.05317

tert-butyl (4-(9H-carbazol-9-yl)butyl)(tert-butoxycarbonyl)carbamate (2) A round-bottom flask was charged with di-tert-butyl iminodicarbonate (1.5 eq. 1.08 g, 3.9 mmol) was stirred with KOH (2 eq. 0.291 g, 5.2 mmol) in DMF (6 mL). After 30 minutes of stirring 9-(4-bromobutyl)-9H-carbazole (0.78 g, 2.6 mmol) was added with additional 3 mL of DMF, heated to 80 °C and stirred overnight. The reaction mixture was cooled down to room temperature and washed with saturated solution of LiCl, washed with brine, extracted using EtOAc, dried over $MgSO_4$. The solvent was removed under reduced pressure. The crude mixture was purified using silica chromatography using Pentane:EtOAc (95:5 v/v %) to obtain the product as white crystal (1.15 g, quantitative yield).

^{1}H NMR (400 MHz, $CDCl_3$) δ 8.1 (d, J = 7.8 Hz, 2H), 7.5 – 7.4 (m, 4H), 7.2 – 7.2 (m, 2H), 4.3 (t, J = 7.2 Hz, 2H), 3.6 (t, J = 7.3 Hz, 2H), 1.9 (p, J = 7.3 Hz, 2H), 1.7 (h, J = 7.4 , 6.7 Hz, 2H), 1.4 (s, 18H). ^{13}C NMR (101 MHz, $CDCl_3$) δ 152.9, 140.5, 125.8, 123.0, 120.5, 118.9, 108.8, 107.8, 82.4, 60.5, 45.9, 42.8, 31.1, 28.2, 26.8, 26.2, 21.2, 14.4. HRMS - ESI^+ (m/z) Calculated for $C_{16}H_{17}BrN$ $[M+H]^+$: 461.24108 Measured: 461.24088

4-(9H-carbazol-9-yl)butan-1-ammonium iodide (3) A round-bottom flask was charged with tert-butyl (4-(9H-carbazol-9-yl)butyl)(tert-butoxycarbonyl)carbamate (2 g, 4.65 mmol) was dissolved in 10 mL of EtOH followed by addition of HI (8 mL, 57 w%) and

left to stir in the dark overnight. The solvent was removed under reduced pressure and redissolved in small amount of EtOH. This was added to a copious amount of Et_2O. The resulting solids were filtered and the procedure was repeated several times to obtain the product as white-off crystals (0.82 g, yield 48 %).

^{1}H NMR (400 MHz, DMSO-d6) δ 8.2 (dd, J = 7.6 , 1.0 Hz, 2H), 7.6 (d, J = 8.2 Hz, 2H), 7.5 (d, J = 19.0 Hz, 3H), 7.5 – 7.4 (m, 2H), 7.3 – 7.1 (m, 2H), 4.4 (t, J = 6.8 Hz, 2H), 2.8 (t, J = 7.6 Hz, 2H), 1.8 (dq, J = 11.2 ,6.9 Hz, 2H), 1.6 – 1.4 (m, 2H).^{13}C NMR (101 MHz, DMSO-d6) δ 140.0, 125.7, 122.1, 120.3, 118.8, 109.3, 41.8, 40.2, 40.0, 39.9, 39.8, 39.7, 39.6, 39.5, 39.3, 39.1, 38.89, 38.7, 25.7, 24.8. HRMS - ESI$^+$ (m/z) Calculated for $C_{16}H_{19}N_2$ $[M+H]^+$: 239.15428 Measured: 239.15399

PEROVSKITE PRECURSOR SOLUTION ($Cs_{0.25}FA_{0.75}Sn_{0.5}Pb_{0.5}I_3$)

The precursor solution was prepared in a vial by mixing CsI (181.86 mg, 0.7 mmol) FAI (361.2 mg, 2.1 mmol), PbI_2 (645.42 mg, 1.4 mmol) SnI_2 (521.6 mg, 1.4 mmol) followed by addition of 2 mL of DMF:DMSO (4:1 v/v% ratio) and stirring overnight. SnF_2 (0.14 mmol was added as additive to retard the oxidation of Sn^{2+} to Sn^{4+}. Prior to deposition the stirred solution was filtered using 0.20 µm PTFE filter.

DEVICE FABRICATION

Devices were fabricated on $30\,mm^2 \times 30\,mm^2$ prepatterned indium tin oxide (ITO) coated glass substrates that were ultrasonically cleaned in detergent solution, deionized water, acetone and isopropanol. After drying them in oven at 140 °C for 10 to 20 minutes the substrates were treated with UV-O_3 for 20 minutes. The monolayer was formed by dipping the cleaned substrates in an 0.1 m M solution of **Br-2PACz** in EtOH that was ultrasonicated for 30 minutes. The follwoing day the substrates were spun for 10 s at 3000 rpm before going on a hot plate at 100 °C for 10 minutes followed by washing using 100 µL of EtOH while being spun at 6000 r to 4000 rpm for 30 s. For the formation of SABs, the samples with the monolayer were covered with 0.5 mg mL^{-1} solution of **4 NH_3CzI** left for 1 m to 2 minutes prior to spinning the sample at 3000 rpm and dried at 100 °C to 120 °C for 1 m to 5 minutes. In both cases of the monolayer and SABs, 100 µL of the active material was spincoated at 4000 rpm for 80 s and at 25 s 250 µL of anisole was added. The sample was heated at 120 °C for 10 minutes. Finally, deposition of C_{60} (20 Å), BCP (30 Å) and Ag (100 nm as the top electrode.

CURRENT DENSITY-VOLTAGE (J-V) MEASUREMENTS

J-V curves were recorded using Keithley 2400 source-meter under simulated *AM 1.5 G* solar illumination using a Steuernagel Solar constant 1200 metal halide lamp in an inert atmosphere. The light intensity was calibrated to 100 mW/cm^2.

EXTERNAL QUANTUM EFFICIENCY (EQE)

The EQE measurements were carried out in an inert atmosphere. The obtained photocurrent was measured using a lock in an amplifier (Stanford Research System, Model SR830 DPS Lock-In Amplifier). A monochromatic light from a xenon lamp was obtained by set of band pass filters with full width at half maximum (FWHM) of 10 ± 2 nm.

ATOMIC FORCE MICROSCOPY (AFM)

AFM topological images were recorded in ScanAsyst Mode on a Bruker Multimode 8 microscope with Scan Asyst Air probes (resonant frequency 70 kHz, spring constant 0.4 N/m) at a scan rate of 0.912 Hz and a resolution of 512 samples per line. The data were analyzed with Gwyddion (Free data analysis software).

SCANNING ELECTRON MICROSCOPY (SEM)

SEM images were recorded in air on a FEI. NovaNano SEM 650 with an acceleration voltage of 18kV. Measurements of the cross section, morphology and grain sizes were performed using A LEO 1530 LEO scanning electron microscope with a in-lens detector operating at 3 kV.

CONTACT ANGLE MEASUREMENTS

The hybrid perovskite solution was used as a dropplet for the measurements Contact angle goniometer with Ossila Contact angle v3.0 was used for surface tension measurements.

BIBLIOGRAPHY

[1] H.-S. Kim, C.-R. Lee, J.-H. Im, K.-B. Lee, T. Moehl, A. Marchioro, S.-J. Moon, R. Humphry-Baker, J.-H. Yum, J. E. Moser, M. Grätzel, N.-G. Park, *Scientific Reports* **2012**, *2*, DOI 10.1038/srep00591.

[2] J. Jeong, M. Kim, J. Seo, H. Lu, P. Ahlawat, A. Mishra, Y. Yang, M. A. Hope, F. T. Eickemeyer, M. Kim, Y. J. Yoon, I. W. Choi, B. P. Darwich, S. J. Choi, Y. Jo, J. H. Lee, B. Walker, S. M. Zakeeruddin, L. Emsley, U. Rothlisberger, A. Hagfeldt, D. S. Kim, M. Grätzel, J. Y. Kim, *Nature* **2021**, *592*, 381–385.

[3] J. Li, H.-L. Cao, W.-B. Jiao, Q. Wang, M. Wei, I. Cantone, J. Lü, A. Abate, *Nature Communications* **2020**, *11*, DOI 10.1038/s41467-019-13910-y.

[4] Y. Jiang, L. Qiu, E. J. Juarez-Perez, L. K. Ono, Z. Hu, Z. Liu, Z. Wu, L. Meng, Q. Wang, Y. Qi, *Nature Energy* **2019**, *4*, 585–593.

[5] B. Conings, A. Babayigit, H.-G. Boyen, *ACS Energy Letters* **2019**, *4*, 873–878.

[6] A. Babayigit, A. Ethirajan, M. Muller, B. Conings, *Nature Materials* **2016**, *15*, 247–251.

[7] B. Hailegnaw, S. Kirmayer, E. Edri, G. Hodes, D. Cahen, *The Journal of Physical Chemistry Letters* **2015**, *6*, 1543–1547.

[8] I. R. Benmessaoud, A.-L. Mahul-Mellier, E. Horváth, B. Maco, M. Spina, H. A. Lashuel, L. Forró, *Toxicology Research* **2016**, *5*, 407–419.

[9] L. Serrano-Lujan, N. Espinosa, T. T. Larsen-Olsen, J. Abad, A. Urbina, F. C. Krebs, *Advanced Energy Materials* **2015**, *5*, 1501119.

[10] A. Filippetti, S. Kahmann, C. Caddeo, A. Mattoni, M. Saba, A. Bosin, M. A. Loi, *Journal of Materials Chemistry A* **2021**, *9*, 11812–11826.

[11] H.-H. Fang, S. Adjokatse, S. Shao, J. Even, M. A. Loi, *Nature Communications* **2018**, *9*, DOI 10.1038/s41467-017-02684-w.

[12] T. Handa, T. Yamada, H. Kubota, S. Ise, Y. Miyamoto, Y. Kanemitsu, *The Journal of Physical Chemistry C* **2017**, *121*, 16158–16165.

[13] R. L. Milot, G. E. Eperon, T. Green, H. J. Snaith, M. B. Johnston, L. M. Herz, *The Journal of Physical Chemistry Letters* **2016**, *7*, 4178–4184.

[14] L. Ma, F. Hao, C. C. Stoumpos, B. T. Phelan, M. R. Wasielewski, M. G. Kanatzidis, *Journal of the American Chemical Society* **2016**, *138*, 14750–14755.

[15] L.-J. Chen, C.-R. Lee, Y.-J. Chuang, Z.-H. Wu, C. Chen, *The Journal of Physical Chemistry Letters* **2016**, *7*, 5028–5035.

[16] B.-B. Yu, Z. Chen, Y. Zhu, Y. Wang, B. Han, G. Chen, X. Zhang, Z. Du, Z. He, *Advanced Materials* **2021**, *33*, 2102055.

[17] S. Hu, K. Otsuka, R. Murdey, T. Nakamura, M. A. Truong, T. Yamada, T. Handa, K. Matsuda, K. Nakano, A. Sato, K. Marumoto, K. Tajima, Y. Kanemitsu, A. Wakamiya, *Energy & Environmental Science* **2022**, *15*, 2096–2107.

[18] J. Cameron, P. J. Skabara, *Materials Horizons* **2020**, *7*, 1759–1772.

[19] M. Kim, M. Yi, W. Jang, J. K. Kim, D. H. Wang, *Polymers* **2020**, *12*, 129.

[20] B. Y. Kadem, M. Al-Hashimi, A. S. Hasan, R. G. Kadhim, Y. Rahaq, A. K. Hassan, *Journal of Materials Science: Materials in Electronics* **2018**, *29*, 19287–19295.

[21] K. Norrman, M. V. Madsen, S. A. Gevorgyan, F. C. Krebs, *Journal of the American Chemical Society* **2010**, *132*, 16883–16892.

[22] S. Wu, S. Han, Y. Zheng, H. Zheng, N. Liu, L. Wang, Y. Cao, J. Wang, *Organic Electronics* **2011**, *12*, 504–508.

[23] K. W. Wong, H. L. Yip, Y. Luo, K. Y. Wong, W. M. Lau, K. H. Low, H. F. Chow, Z. Q. Gao, W. L. Yeung, C. C. Chang, *Applied Physics Letters* **2002**, *80*, 2788–2790.

[24] S. Adjokatse, J. Kardula, H.-H. Fang, S. Shao, G. H. ten Brink, M. A. Loi, *Advanced Materials Interfaces* **2019**, *6*, 1801667.

[25] M.-G. Baek, J.-E. Shin, D.-H. Hwang, S.-H. Kim, H.-G. Park, S.-G. Park, *Crystals* **2020**, *10*, 645.

[26] S. A. Paniagua, P. J. Hotchkiss, S. C. Jones, S. R. Marder, A. Mudalige, F. S. Marrikar, J. E. Pemberton, N. R. Armstrong, *The Journal of Physical Chemistry C* **2008**, *112*, 7809–7817.

[27] C. D. Bain, E. B. Troughton, Y. T. Tao, J. Evall, G. M. Whitesides, R. G. Nuzzo, *Journal of the American Chemical Society* **1989**, *111*, 321–335.